

REPORT DOCUMENTATION PAGE

*Form Approved
OMB No. 0704-0188*

Public reporting burden for this collection of information is estimated to average 1 hour per response, including the time for reviewing instructions, searching existing data sources, gathering and maintaining the data needed, and completing and reviewing this collection of information. Send comments regarding this burden estimate or any other aspect of this collection of information, including suggestions for reducing this burden to Department of Defense, Washington Headquarters Services, Directorate for Information Operations and Reports (0704-0188), 1215 Jefferson Davis Highway, Suite 1204, Arlington, VA 22202-4302. Respondents should be aware that notwithstanding any other provision of law, no person shall be subject to any penalty for failing to comply with a collection of information if it does not display a currently valid OMB control number. **PLEASE DO NOT RETURN YOUR FORM TO THE ABOVE ADDRESS.**

1. REPORT DATE (DD-MM-YYYY) 31-08-2006		2. REPORT TYPE Journal Article		3. DATES COVERED (From - To)	
4. TITLE AND SUBTITLE Wave Front Sensor for Solar Concentrator Control (Preprint)				5a. CONTRACT NUMBER	
				5b. GRANT NUMBER	
				5c. PROGRAM ELEMENT NUMBER	
6. AUTHOR(S) Joseph N. Beasley (AFRL/PRSO)				5d. PROJECT NUMBER 10110062	
				5e. TASK NUMBER	
				5f. WORK UNIT NUMBER	
7. PERFORMING ORGANIZATION NAME(S) AND ADDRESS(ES) Air Force Research Laboratory (AFMC) AFRL/PRSO 8 Draco Drive Edwards AFB CA 93524-7135				8. PERFORMING ORGANIZATION REPORT NUMBER AFRL-PR-ED-JA-2006-299	
9. SPONSORING / MONITORING AGENCY NAME(S) AND ADDRESS(ES) Air Force Research Laboratory (AFMC) AFRL/PRS 5 Pollux Drive Edwards AFB CA 93524-70448				10. SPONSOR/MONITOR'S ACRONYM(S)	
				11. SPONSOR/MONITOR'S NUMBER(S) AFRL-PR-ED-JA-2006-299	
12. DISTRIBUTION / AVAILABILITY STATEMENT Approved for public release; distribution unlimited (AFRL-ERS-PAS-2006-223)					
13. SUPPLEMENTARY NOTES Submitted for publication in IEEE Transactions on Aerospace and Electronic Systems					
14. ABSTRACT This article is the culmination of research directed into finding a system to control the position of the focal spot of paraboloid concentrators for use in terrestrial and space solar concentration applications. After a brief introduction into the area of study, the article describes how a normal Shack-Hartmann wavefront sensor is modified for use in detecting and tracking the focal spot. The first experiment describes how the wavefront sensor is to be utilized in a solar application and shows the adjustment from lenslets to cylindrical mirrors on a thruster. Next, the paper details the analysis and development of the algorithms used in locating the focal spot on a thruster absorber utilizing a correlation method and an area centroid method. The article concludes with a paragraph on suitable future work.					
15. SUBJECT TERMS					
16. SECURITY CLASSIFICATION OF:			17. LIMITATION OF ABSTRACT A	18. NUMBER OF PAGES 64	19a. NAME OF RESPONSIBLE PERSON Dr. Michael R. Holmes
a. REPORT Unclassified					19b. TELEPHONE NUMBER (include area code) N/A
b. ABSTRACT Unclassified					
c. THIS PAGE Unclassified					

Wavefront Sensor for Solar Concentrator Control

(PREPRINT)

ABSTRACT

This article is the culmination of research directed into finding a system to control the position of the focal spot of paraboloid concentrators for use in terrestrial and space solar concentration applications. After a brief introduction into the area of study, the article describes how a normal Shack-Hartmann wavefront sensor is modified for use in detecting and tracking the focal spot. The first experiment describes how the wavefront sensor is to be utilized in a solar application and shows the adjustment from lenslets to cylindrical mirrors on a thruster. Next, the paper details the analysis and development of the algorithms used in locating the focal spot on a thruster absorber utilizing a correlation method and an area centroid method. The article concludes with a paragraph on suitable future work.

Index Terms - Algorithms, Control Systems, Solar Energy, Solar Satellites, Space Vehicle Control, Space Vehicle Propulsion.

INTRODUCTION

For direct thrust solar thermal propulsion (STP) or terrestrial solar heating using concentrators, proper positioning of the solar focal spot is paramount. Along with positioning information, a sensor system must tolerate the intense heat generated by a solar concentrator. The sensor system developed in this article satisfies both of the previous requirements. The system developed in this article utilizes the thruster - absorber as the focal spot sensor with a Charge Coupled Device (CCD) camera to image the absorber - sensor. Two image processing methods are applied to the CCD images to generate the focal spot location. Once the focal spot is located on an image, positioning information and commands are generated to reposition the concentrators. Both methods produce the focal spot information needed to generate positioning information for the concentrator.

Solar Thermal Propulsion Background

The solar concentrator field may be divided into two primary areas of interest: terrestrial-based and space-based. Both types of concentrator can be either imaging or non-imaging and they can be rigid or inflatable. Other applications include terrestrial power, space power, materials processing, hazardous material destruction, building illumination, and space plant illumination.

Solar Thermal Power as propulsion has its roots in the work of Krafft Erick's Solar Powered Spaceship done in 1956. Erick's spaceship was the first design that utilized a double solar concentrator connected together by a hydrogen powered thruster. Further development of the solar powered spaceship concept was sporadic during the 1950's and 1960's until a single concentrator thruster was developed in 1963. After 1963, the next development of the technology occurred in 1979 with the development of a twin off axis paraboloid concentrator concept, by Rocketdyne. The solar thermal field was then relatively dormant from 1979 until the Rocketdyne thruster tests of 1984-1991 with a new Rhenium coil cylindrical cavity.

The solar thermal propulsion activity really took off in the 1990's with the development of castable thin films

for casting inflatable concentrators. The 1990's also saw the development of rigidized structures for constructing the support structures for inflatable solar concentrators. The year 1997 saw the successful deployment of a 2 X 3 meter inflatable concentrator that signaled that the technology was ready for scaling up. The development activity from 1997 onward has been dominated by the difficult task of the manufacture of a mandrel for casting a 4 X 6 meter inflatable concentrator.

The major difference between a chemical-type thruster or spacecraft and an STP thruster or spacecraft is that the STP spacecraft does not carry the added weight of the oxidizer as the chemical spacecraft. Since the energy for propulsion is available to the spacecraft in orbit, in the form of sunlight, an STP system would not have to carry both propellant and oxidizer to produce energy for the upper stage unit. Only an atomic or molecular propellant such as hydrogen would be needed on the upper stage. Thus, the STP has a weight advantage over the chemical spacecraft in that a lighter molecular weight propellant is used.

The STP system heats up hydrogen in the thruster/absorber and then expands the hydrogen through a nozzle to produce the thrust required by the vehicle. Thus the thrust-to-mass(propellant) efficiency of the STP system

is much better (more than two times better) than the equivalent chemical upper stage as less non-payload mass is needed in the STP system for the same amount of thrust to be developed. [1] Specific Impulse or I_{sp} is the rocket propulsion term that measures the thrust per unit of propellant expended. Thus STP systems have a much higher I_{sp} than chemical systems of the same size.

The STP system also has the added task of controlling the solar concentrators within spacecraft constraints. Not only does the spacecraft need to properly point the concentrators towards the Sun while the craft maneuvers in space, it needs to protect them from the exhaust of the spacecraft. These two requirements limit the control region of the concentrators, thus possibly limiting the available power or limiting maneuverability of the spacecraft itself. One final control requirement is that the focal cone should always be positioned on the aperture closest to the nozzle for effective heat transfer to the propellant. [2]

The current Air Force Research Laboratory (AFRL) concept for the concentrators for a solar thruster is two off axis paraboloid concentrators connected to a central thruster. See Fig. 1.

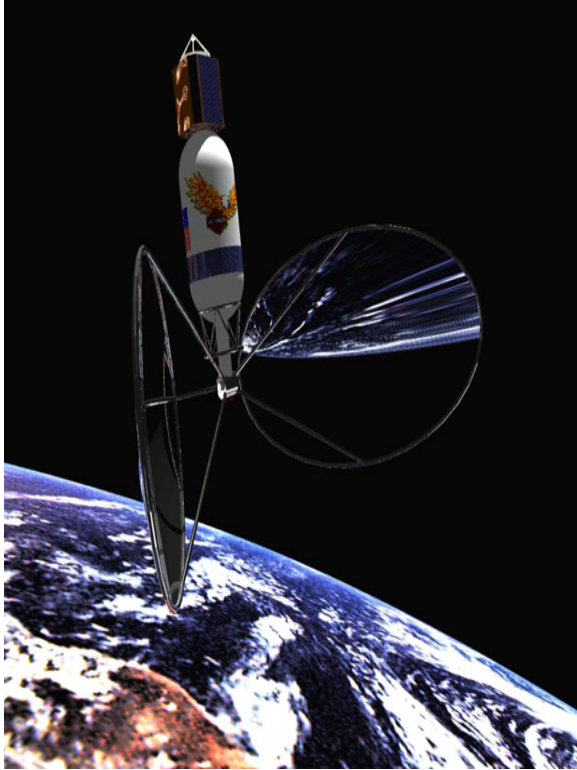


Figure 1 Solar Thermal Configuration.

Each concentrator is connected to the central thruster with a hexapod or Stewart Platform offering 6 degree of freedom (DOF) control. The 6 DOF needed are yaw, pitch, roll, x, y, and z. Coarse alignment is obtained using an on axis detector, such as a Sun tracker or photodiode, which brings the spacecraft and concentrators into a general alignment with the Sun. Coarse alignment brings the focal cone into rough alignment with the desired aperture on the thruster. [3] Concentrator control should provide optimum energy transfer to the solar thruster while

protecting the concentrator and spacecraft from the dynamic behavior of the whole system.

Focal Spot:

Proper tracking of the Sun or proper positioning of the focal spot ensures maximum energy transfer to the propellant. To properly track the Sun for maximum heat transfer, the controller requires a sensor with enough resolution to ensure proper control or better optimal control for maximum heat transfer.

The new sensor is shaped like a cone and serves not only as the sensor but also as the solar heat absorber to transfer heat to the propellant. The method of determining where the focal spot is located using the new sensor is based on the method used in a Shack-Hartmann optical wave front sensor.

Solar Sensor Options [4],[5]

Most terrestrial Sun trackers were developed to track the Sun from the Earth and rely on open loop mechanical tracking algorithms. That is, tracking then was based on mechanical position. Relying on open loop control these systems were prone to error, because they lacked Sun position error and inertial reference feedback. The open

loop control systems are also unable to handle the strut length thermal dependence that feedback systems are able to overcome.

Solar sensors are categorized as mechanical, thermal, or visual. Mechanical sensors were discussed in the previous paragraph. Thermal based sensors, such as the normal incident pyrheliometer, pyranometer, and calorimeter, black-bodies, and radiometers rely on thermopiles or thermocouples to measure the temperature rise or temperature difference between the sensor and its environment.

Photodiodes and photocells are electronic sensors that are neither mechanical nor thermal that can be used as replacements for thermocouples or thermopiles in other devices. Photodiodes consist of a Silicon diode in a container that exposes the PN junction to incident light. These devices operate on the internal photoelectric effect. Photocells are also Silicon-based and are usually operated at short-circuit current. Both photocells and photodiodes are used to detect visible light.

Solar Sensor Problem Statement

To be useful as a solar sensor especially in space, the sensor cannot rely on Earth coordinates for tracking

information. The sensor also must be able to handle the high temperatures involved with a solar concentrator that concentrates the sunlight to temperatures approaching 3100 degrees Kelvin on the absorber.

The research problem is to: (1) develop a sensor that provides information about the location of the focus beam from the concentrator that also can tolerate the extreme temperatures involved in providing solar heating, and (2) develop the mathematics of a control system that will focus the concentrator in an optimal fashion based on the sensor measurements.

The thermal based sensors described in the previous section, except for the black bodies and calorimeters, are not able to operate at the extreme temperatures expected within the STP system. Also, photodiodes and photocells do not have the temperature capabilities necessary to directly be used as a focal spot sensor. Photo devices are limited to a temperature of about 85 degrees C.

A black body or cavity radiation sensor would not be useful to sense the focal spot as the thruster does not have a cavity on board. A black body or cavity sensor is better suited to a thruster that utilizes stored energy for propulsion and does not have a need for continuous thrust.

Also, calorimeters tend to block the light from entering the thruster/absorber.

The sensor developed solves the temperature issue by using the absorber as a Wave Front Sensor for focal spot determination. This sensor overcomes the thermal limitations of the other sensors by using the reflections of the concentrated light in the sensor as the tracking information. Since the absorber has to take the high temperatures of the concentrated sunlight, it is already capable of handling the temperature requirements. The CCD images the absorber to determine the location of the focal beam based on shape, size, and location of the reflections on the absorber. Additionally, the thrust could be monitored and used as a feedback mechanism to enhance the control of the focal spot.

WAVEFRONT SENSOR

The Hartmann wave front sensor was developed by Hartmann in 1900 and was used for checking optical telescopes for aberrations. It was an array of holes in a plate placed in front of the mirror of the telescope being checked so that light tubes from the array would impinge on the telescope mirror. Two photographic plates were used to

collect the light information. One plate was placed just before the focal spot of the telescope and the other one was placed just behind the focal spot. The distance between the plates was chosen so that the light rays would be separated from each other. The path of the light rays was traceable by measuring the centroids of the two images. Thus, Hartmann was able to determine figures of merit for various large telescopes. [6]

Dr. Roland Shack developed the method of replacing the holes of the Hartmann sensor with small lenses or lenslets to improve the capability of the Hartmann sensor when taking images of satellites or stars at the same time as the wavefront phase error was being determined. The method was developed while solving a problem with imaging satellites and stars from the Earth. Dr. Aden Mienel's solution was to determine the Optical Transfer Function of the atmosphere at the same time as the image being taken. The Hartmann sensor was not satisfactory as Mienel could not allow the array to cover the aperture of the telescope because it would eliminate the image of the satellite in favor of determining wavefront tilt over the imaging of the satellites. Mienel tried to use a beam splitter to take Hartmann images while taking images of the satellites and stars. This method suffered from the weak intensity images

of the light rays in the Hartmann sensor. Shack suggested that replacing the apertures in the Hartmann sensor with lenses would eliminate the problems that Mienel was having with his Hartmann device. The lenslets focused spots onto an image plane such that the displacement of the spots from the ideal position of the spots indicated wavefront tilt.

[7] Thus, the Shack-Hartmann system overcame the shortcomings of the Hartmann sensor while increasing the sensitivities of the Hartmann device alone. A comparison of the two systems is depicted in Fig. 2. The Shack-Hartmann sensor is not suitable for use in tracking the focal spot of concentrated solar rays because of the high temperatures encountered in a concentrated sunlight application. As with other sensors, lenslets would suffer from the effects of concentrated light and from contamination of hot absorber vapors.

The wavefront sensor described in this article utilizes the tubing of the absorber as mirrors that collect information about the light scattered on the sensor from the concentrator. In this manner, the tubes take the place of the holes or lenslets of the Hartmann or Shack-Hartmann wavefront sensor. With the previous introduction and background information, a progression of topics documenting the development of the sensor described in this article

will be presented, beginning with a discussion of cylindrical mirrors and their use as a wavefront sensor in the sensor/absorber.

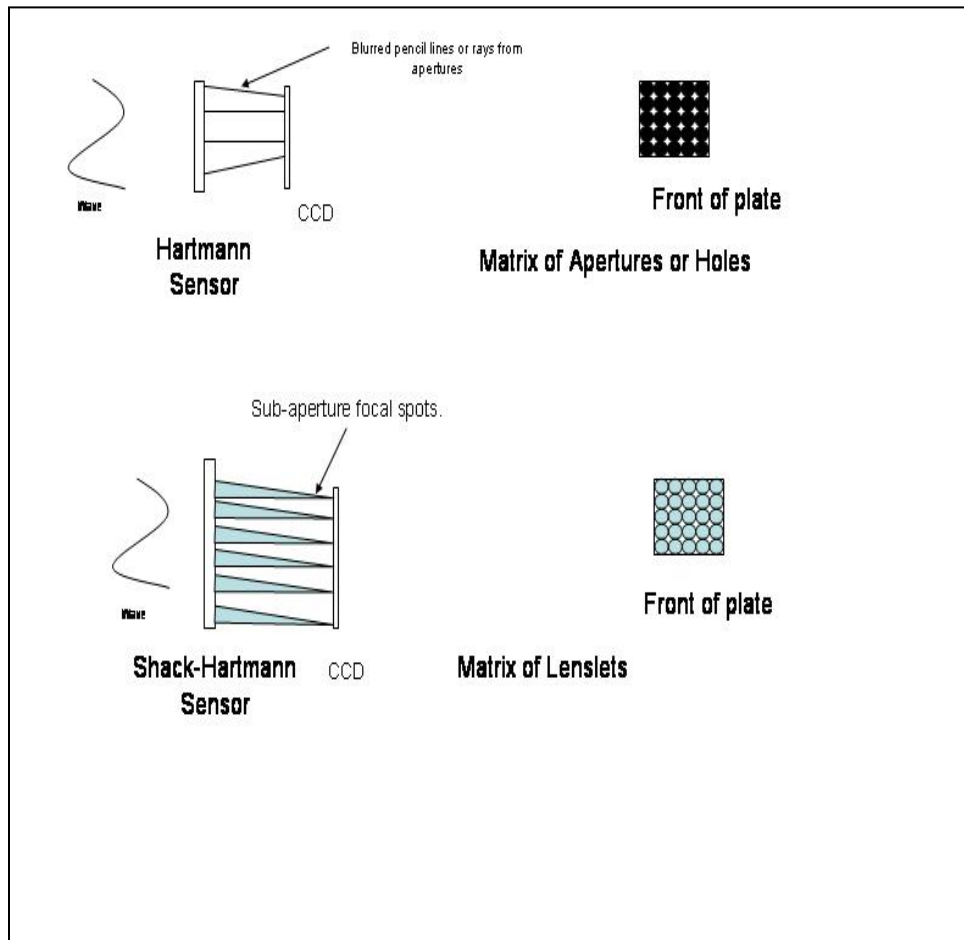


Figure 2 Wave Front Sensor Comparison

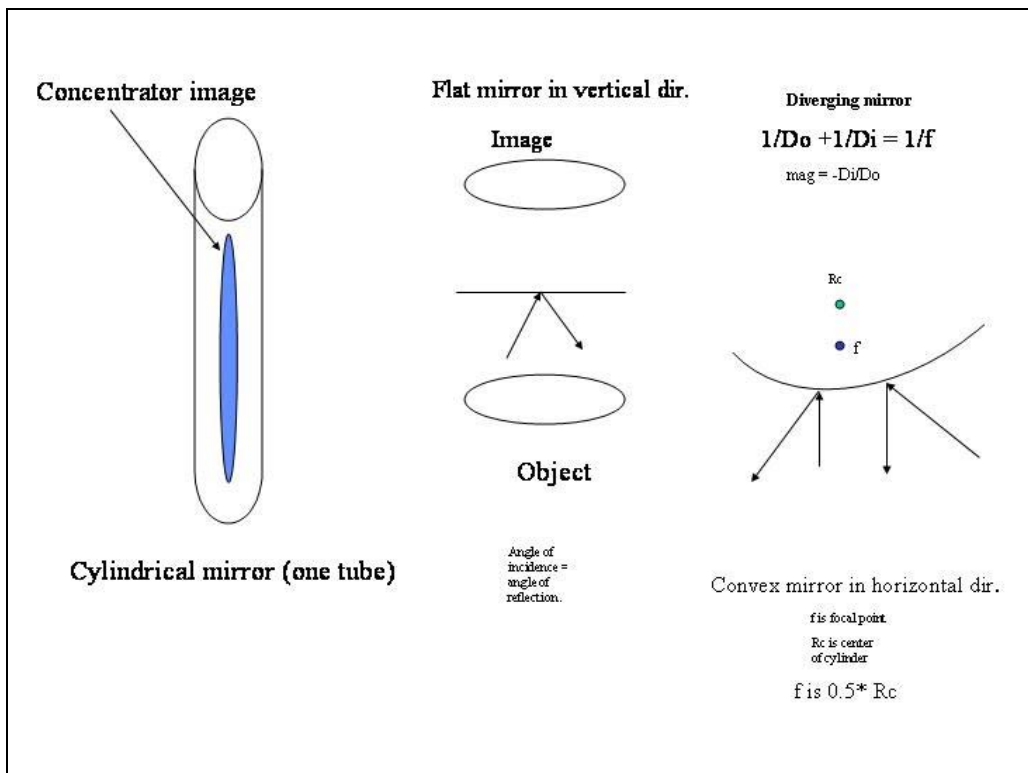


Figure 3 Cylindrical Mirror

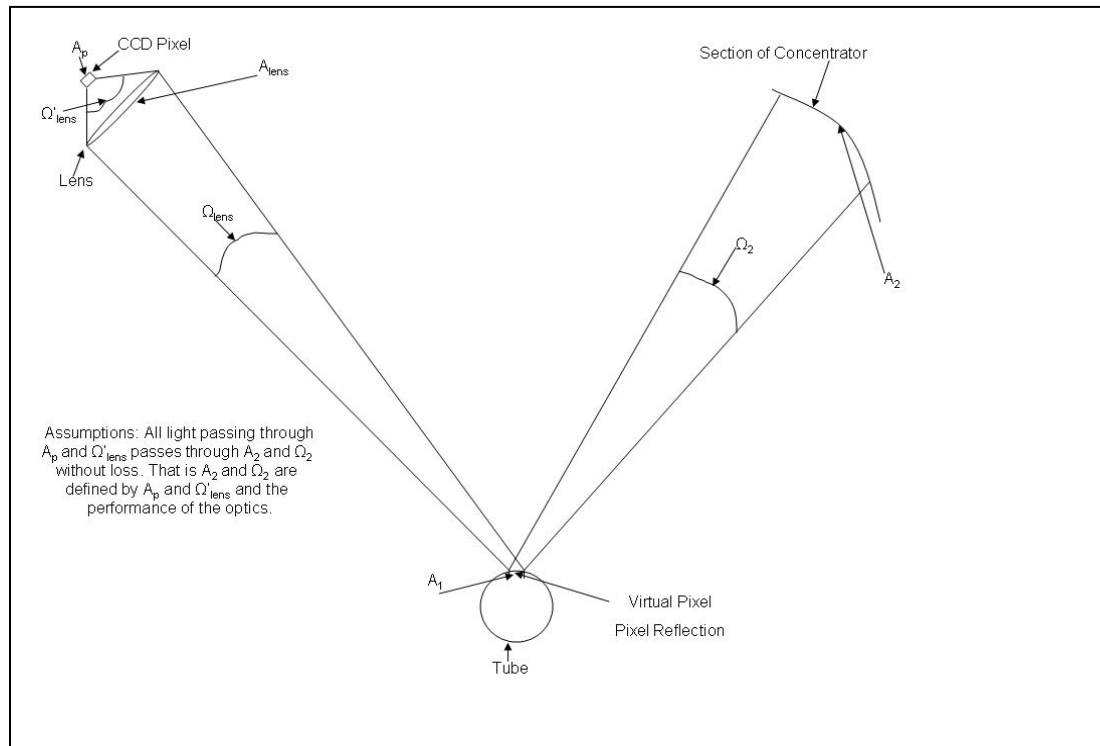


Figure 4 Flux Tube Construction

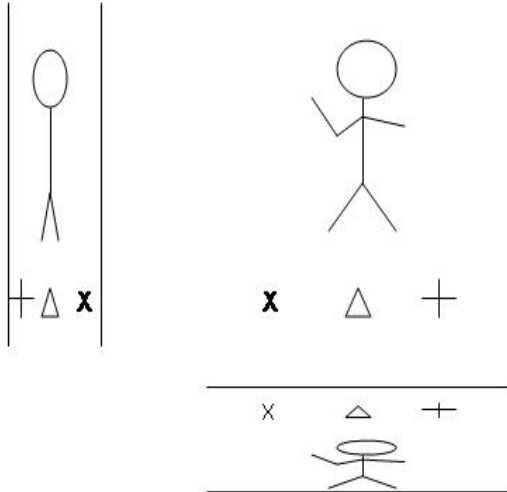


Figure 5 View Of Figures In Cylindrical Mirror From Camera

CYLINDRICAL MIRRORS

Since the sensor for this application uses coiled tubing as its primary configuration, a brief review of cylindrical mirrors is necessary to understand the reflections generated by the conical tubing absorber. Fig. 3 shows the normal situation encountered with the use of a cylindrical mirror. In general a cylindrical mirror will tend to compress an object's reflection along the length of

the mirror. An object's reflection also tends to get larger as the object moves towards the mirror.

Fig. 3 also shows the reflections from the cylindrical mirror along two of its axes. In one axis, in the straight on view, the cylindrical mirror acts like a flat mirror with the light rays adhering to the rules for a flat mirror. That is, incident light is reflected such that the reflected ray returns from the mirror as if it originated at a point behind the mirror, at equal distances to the object; this is also a virtual image. Or the reflection occurs such that the reflected ray's angle is equal to the angle of the incident ray. On the other axis of the mirror, reflections follow the rules of a convex mirror. That is, the mirror surface has a virtual focus point and all of the reflected light rays appear to come from that focus point behind the mirror surface. Reflections from other portions of the cylindrical mirror are more complex than the reflections just discussed, however, the overall effect is that the reflection in the cylindrical mirror is compressed along its main axis and appears larger as the viewer moves closer to the mirror.

The flux tube construction shown in Fig. 4 was used to determine the ability of the CCD pixels to discern changes in light on the concentrator due to misalignment via the

sensor mirrors. A concentrator that is on focus would have light filling all of the concentrator as seen by an observer located at the focus. The sensor or observer in the present case is the absorber/sensor developed in this article.

Since we assume that we don't lose light from the flux tubes, then the pixels should see the same intensity from the tube path as it sees looking directly at the Sun. Also, we assume that our optical system is perfect without any loss of light from the flux tubes due to transmission losses or reflection losses. With the construction presented in Fig. 4 illustrates that with perfect optics, the light intensity on a pixel via the concentrator mirror path is identical to the light intensity that the pixel would receive by direct viewing of the Sun. All virtual pixels whose solid angle fell within the 30 degree half-angle of the cone would have full intensity light on them. Therefore, any pixel intensity value less than direct Sun intensity and whose solid angle fell within the cone of light of the concentrator would indicate misalignment of the concentrator. If the pixel was at or beyond the angle of the cone of the concentrator, that pixel would then be considered a border pixel and would not have full intensity.

Fig. 5 shows a schematic of the camera view of the cylindrical mirror formed by the tubing. This Fig. indicates how a CCD matrix would view the reflection in the tubing.

SENSOR DESCRIPTION

The absorber used as a model sensor consists of a conical shaped absorber made from one quarter inch ($\frac{1}{4}$ ") metal tubing. For actual power conversion, the tubing would be made from a high temperature metal such as Rhenium or Tungsten. The lens or optic system positions the CCD array to virtual focal spots located behind the conical absorber. The tubes from the conical absorber act like cylindrical mirrors (toroidal mirrors) in reflecting the sunlight from the concentrator to the CCD. The virtual location is important in applying the principles from wave front sensing, since the CCD array cannot physically be located behind the mirrors or tubing. In the current case, the lens system then virtually or mathematically positions the array behind the absorber in a manner similar to the Shack-Hartmann system. Each tube would have its own corresponding subset of virtual pixels mapped directly onto the CCD array. These subsets would not overlap. Fig. 6

shows the schematic of the thruster and concentrator with a view of the light in the concentrator as seen by the tubes of the absorber.

The major difference between the method being presented in this article and the Shack-Hartmann system is that the new sensor tries to maximize the number of wave fronts to determine focal spot location, whereas, the Shack-Hartmann system is normally used to optimize one particular wave front.

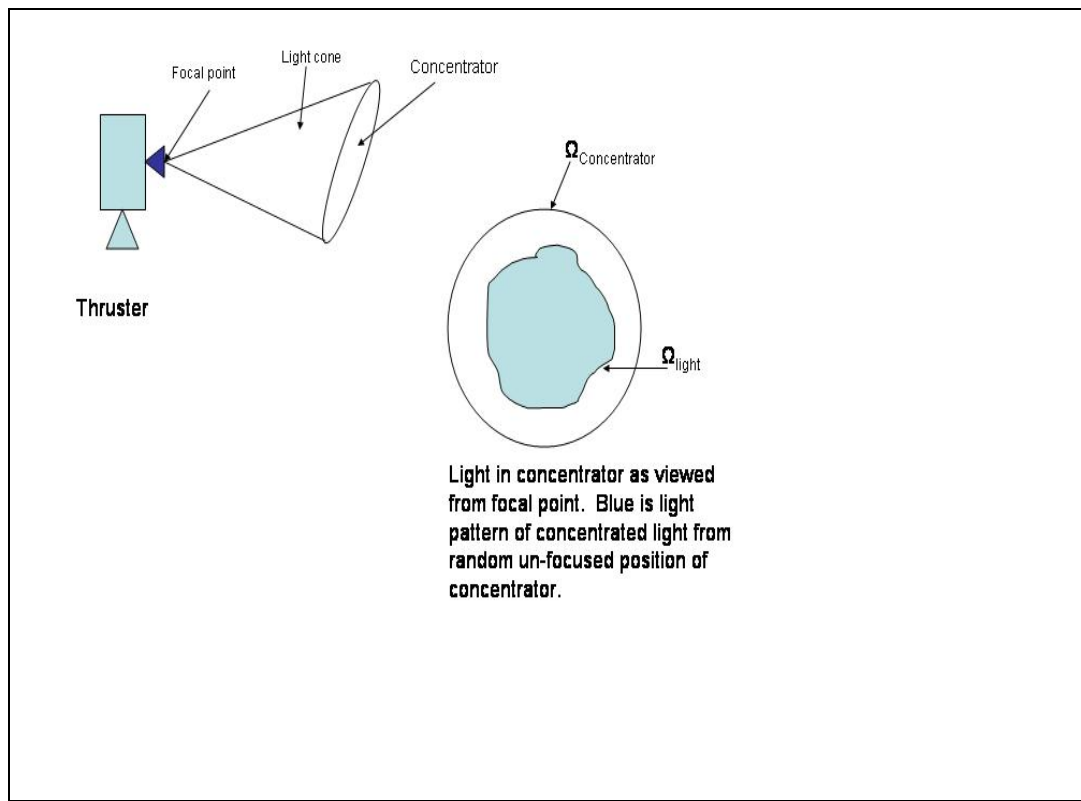


Figure 6 Light In Concentrator

ALGORITHM

Each image taken would be processed by utilizing profile information along diagonal lines representing the four quadrants of the circle (along the 45 degree angles, say). The areas of maximum intensity would be determined along each profile line. The maximums should occur roughly where the tubes appear in the image as that is where pixel virtual images are located. The difference between these areas should give an indication of the direction to the focal spot (almost a centroiding operation on the maximum areas in the image).

By knowing where the center of the absorber is located with respect to the camera (a non-trivial assumption as the camera would probably be mounted to one of the concentrator's movable struts), the controller should be able to generate x, y, z, roll, pitch, and yaw commands for the hexapod controller to move the concentrator to a new position to provide better focus and thus better heating.

Fig. 7 shows the schematic of the proposed sensor solution.

Schematic of Proposed Solution

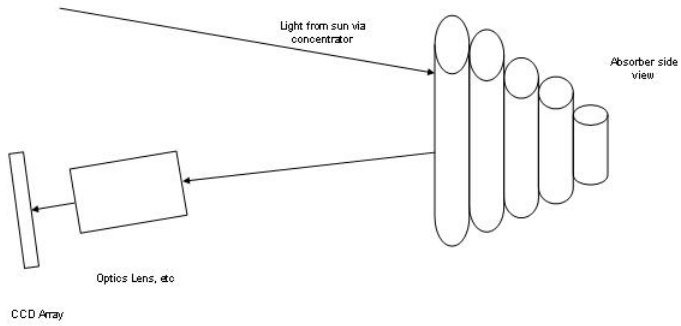


Figure 7 Schematic

For the development of the method presented in this article, stainless steel $\frac{1}{4}$ inch tubes were used for preliminary imaging, while a copper conical absorber with water-cooling if needed will be used for refinement of the method. Fig. 9 shows the stainless steel tubes and Fig. 8 presents the water-cooled conical shaped absorber as shown in the schematic in Fig. 7. The fluid to be heated is flowed through the absorber tubing and heated by the concentrated light.



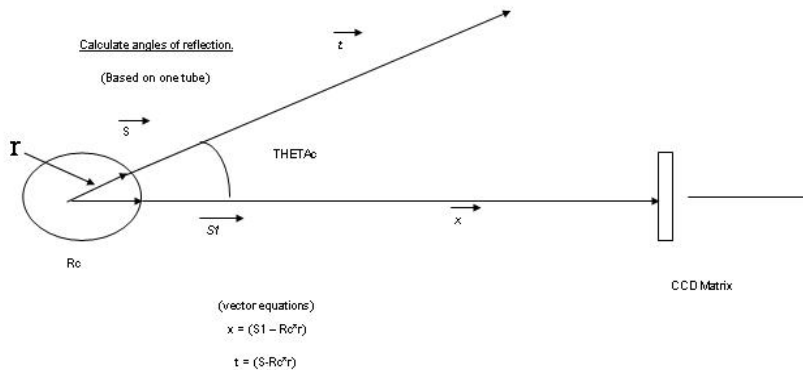
Figure 8 Conical Absorber Sensor



Figure 9 Stainless Steel Tubes

CALCULATIONS

Ray tracing using vectors was used to determine whether the image of the 7-inch diameter concentrator model would reflect off of the tubes and into the aperture of the CCD camera. Fig. 10 illustrates the situation and the equation shown could be used in an iteration to find the angular extremes that would in fact be imaged in the CCD camera. The figure indicates a theta angle that would in fact be double the angle with respect to the normal vector at the surface of the cylinder. This is happening because of the way things were drawn in Fig. 10 and the Law of Reflection: the angle of incidence is equal to the angle of reflection. A quick calculation using just the rays from the extremes of the concentrator model using the Law of Reflection showed that the CCD matrix or camera was able to view all of the reflection of the concentrator model from the tubes.



THETAc is the angle we are trying to find.

$$X \cdot A \cdot X = t \cdot r / \|t\|$$

Figure 10 Vector Calculation for Reflection into CCD

The field of view of the CCD camera was determined to be 1.4 (495 rows) X 2 (657 columns) inches at a distance of 1 meter from the tubes and can.

EXPERIMENT SETUP

A schematic of the experimental set is shown in Fig. 12 and a photo of the experimental equipment is shown in Fig. 11.



Figure 11 Photo Of Test Setup

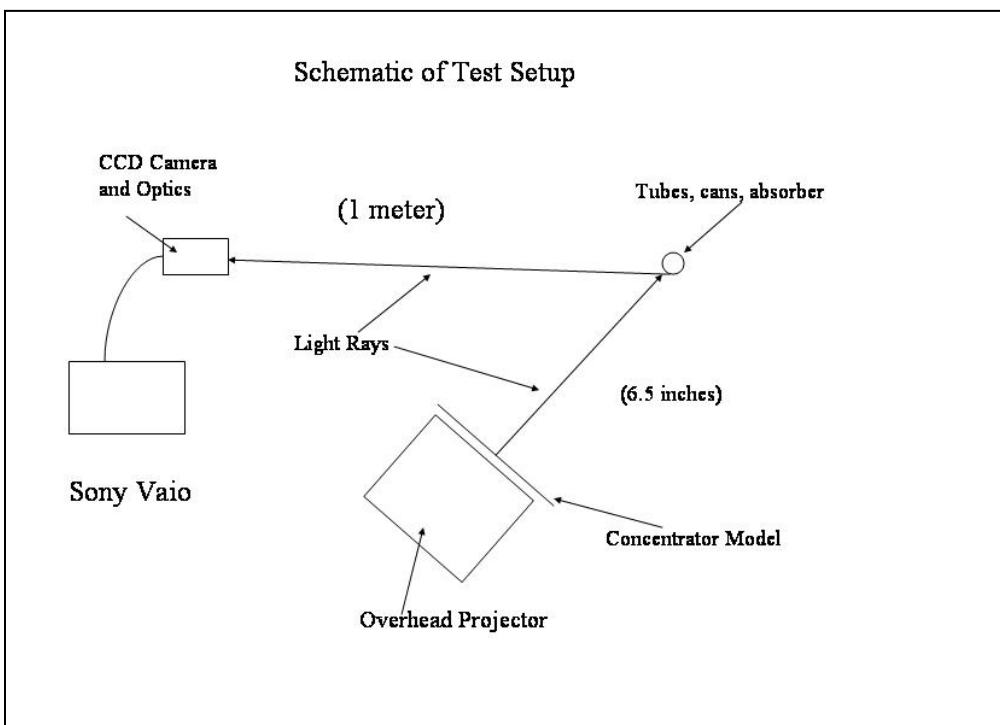


Figure 12 Schematic Of Test Setup

The CCD camera used was an ST237 CCD camera manufactured by Santa Barbara Instrument Group. A 657 by 495 CCD matrix with 7.4-micrometer pixels characterizes the ST237 CCD camera. A very small aperture, to gain depth of field and a 100 mm lens form the optics for the camera. For the experiments discussed in this paper it is focused for objects located one meter away from the lens.

The concentrator model consisted of a 7-inch diagonal circle of white surrounded by a black mask (see Fig. 13, Fig. 14, and Fig. 15). At the distances shown in Fig. 12, the concentrator half-angle model was approximately 7 inches in diameter. A standard overhead projector was used to supply light to the concentrator model using a back projection method.

Images of the stainless steel tubes were taken to discern whether an image of the full view concentrator model could be viewed in the tube. Several different exposure times were used as well as different concentrator patterns from full white circles to circles with varying amounts of area blackened to represent various stages of misalignment. The experiment proceeded by first using one vertical tube and then two vertical tubes.

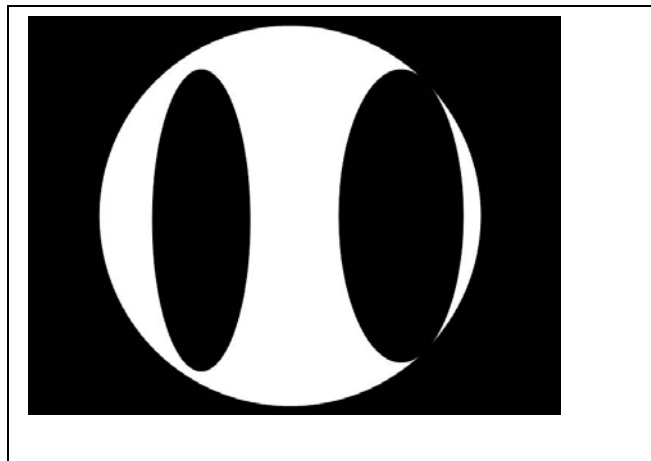


Figure 13 Pattern 1

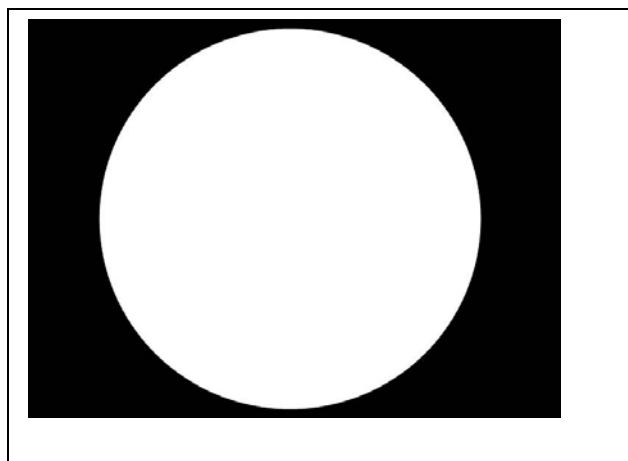


Figure 14 Full Model

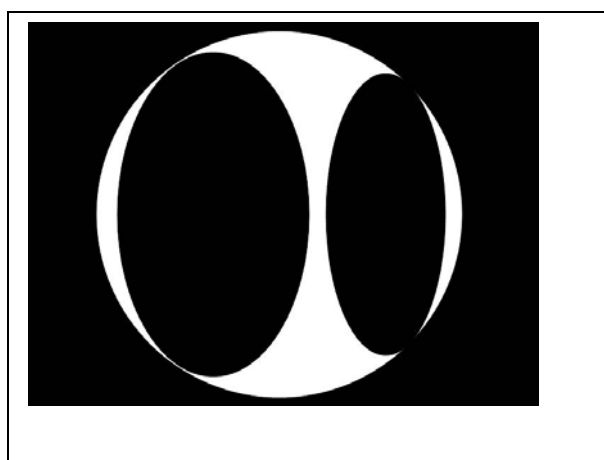


Figure 15 Pattern 2

ONE TUBE

The single tube images indicated that our camera might not have enough resolution to be able to discern between concentrator pattern images. Fig. 17 shows the image of one tube with the full concentrator pattern, and Fig. 16 shows the profile through the image. The images and profiles of the images indicated very little differences between the patterns. The single tube experiment was supposed to show a complete, although distorted image of the concentrator light. At the resolution of the camera, 7.4um pixels focused at 1 meter away from the cylinder did not allow a complete picture of the concentrator model. This experiment may need to be repeated after a camera with higher resolution is acquired.

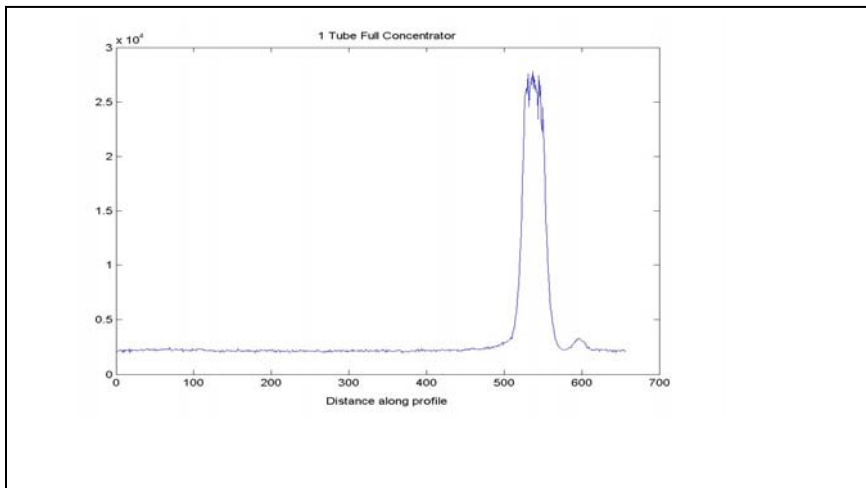


Figure 16 Profile For Figure 17

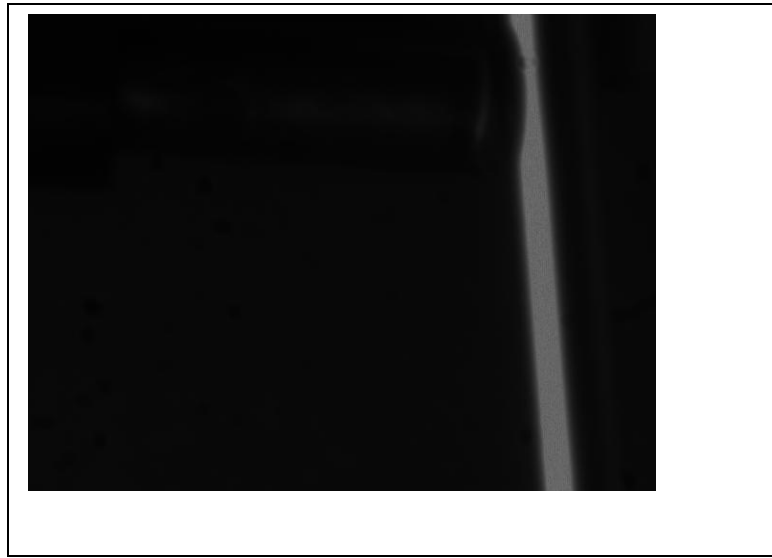


Figure 17 One Tube, Full Concentrator

TWO TUBES

The image from the two-tube experiment is shown in Fig. 19 and its profile is shown in Fig. 18. When the pattern's image and profile are examined, the profiles showed a distinct lowering of the peak intensities seen at each tube location. This result indicated that the concept of the new sensor would work as thought. However, since the patterns were not directly related to actual misalignment of the concentrator, no actual position information could be derived from the profile information.

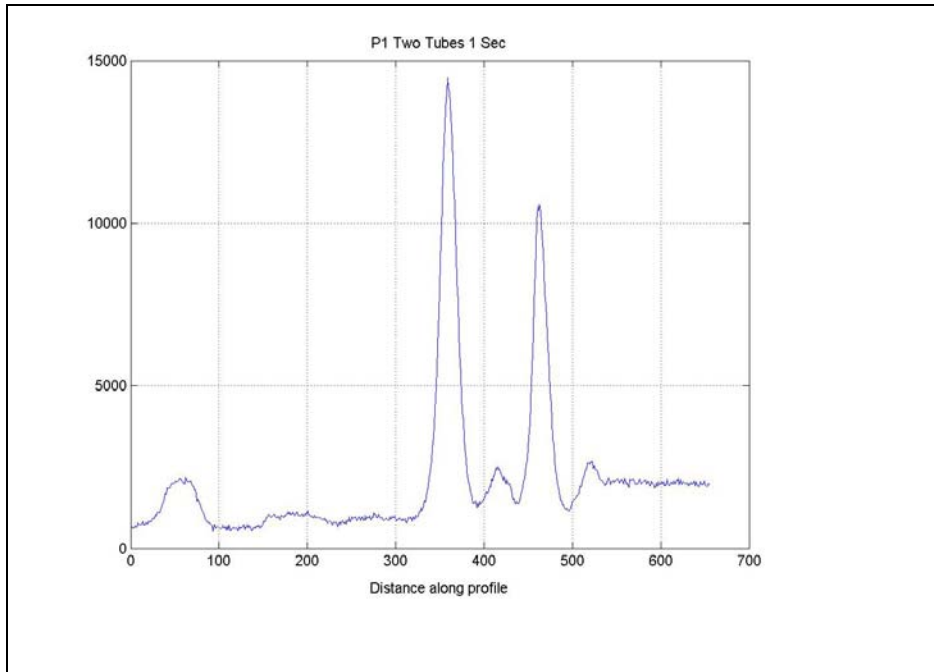


Figure 18 Profile 2 Tube, Pattern 1

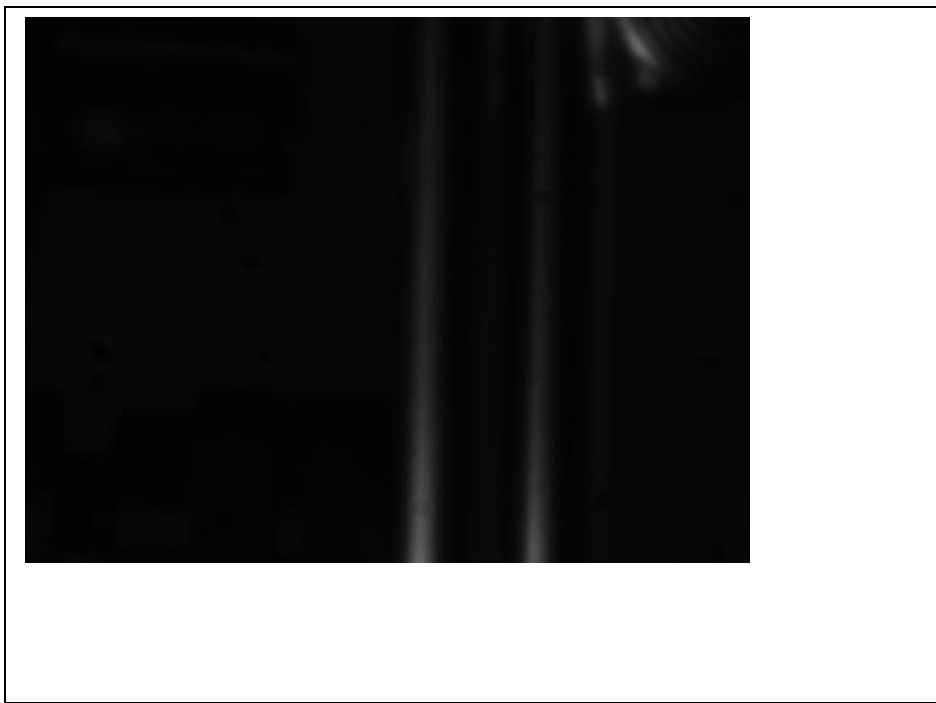


Figure 19 2 Tubes, Pattern 1

EXPERIMENT SUMMARY

From the experiment conducted for this article, the concept of using the cylindrical mirrors of the tubing for the absorber as a wavefront sensor appears to be feasible and correct. The method of using one tube to look at the concentrator model revealed the fact that the CCD camera being used does not have enough resolution to image the concentrator reflection at 1 meter. The two-tube experiment showed a very promising pattern in that it showed a decrease in intensity in conjunction with a reduction in the white areas (Ω_{light}) from the full concentrator ($\Omega_{\text{concentrator}}$) to the other patterns. Since the patterns did not represent actual misalignment, further work would be needed to make suitable patterns to represent misalignment.

WAVEFRONT ALGORITHM DEVELOPMENT

Since the paper [8] presents the hardware being used for focal spot tracking in detail, a brief summary of the components will now be presented for use in this article. The schematic of the hardware is shown in Fig. 20 and consists of a CCD camera, 1 X 2 meter elliptical

concentrator and a conical shaped tubular absorber. A simulator consisting of a 3 inch diameter LED taillight was used to represent the Sun's disk at the Earth's orbit for the 1 X 2 meter concentrator shown in Fig. 20. The actual value of the solar disk at Earth's orbit is 5 inches, so the 3 inch disk in the simulation provided an actually more stringent requirement than the operational STP system. The Sun simulator was mounted on a tripod that allowed various movements of the Sun from on focus to 3-4 diameters off of on focus for imaging and analysis. Putting the Sun simulator at the second focus of the concentrator allowed for simulation of the overall STP system in a laboratory environment using various misalignments off of the second focus point situations to be simulated.

Test Apparatus

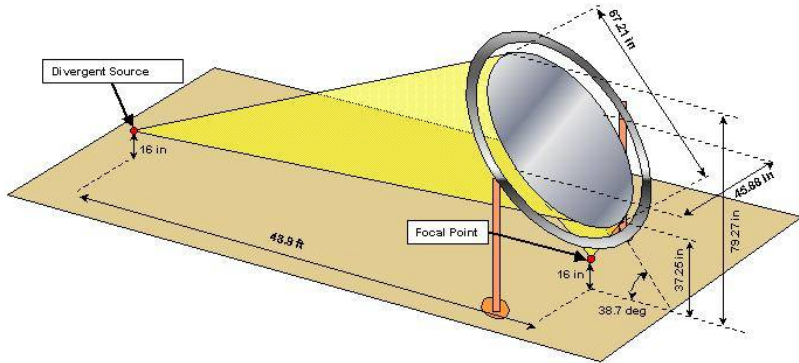


Figure 20 Test Setup

The new algorithms are based on the Shack-Hartmann wave front sensor. The holes and lenslets are replaced by the cylindrical mirrors of the absorber in the current system. Sunlight reflecting on the absorber tubing is imaged by the camera for analysis instead of imaging the array of holes or lenslets of the Shack-Hartmann device. The thruster tubes serve as high temperature mirrors. The absorber takes the heat from the sunlight and conducts it to the hydrogen gas for use in providing thrust. Differences in location of light and how much light is reflected from the tubes are used to determine the focal spot location error for use in a feedback control system.

Two or possibly three different algorithms will be used to locate the focal spot error from the images of the tubes. Different algorithms were deemed necessary because of the 0.1 degree arbitrary control requirement and not having one universal algorithm that covered the three regimes of focus (sunlight more than 5 diameters off focus), intermediate focus (approximately 5-3 diameters off focus), and fine focus (2-1 diameters off focus).

The previous experiment and discussion presented the idea of using the absorber of the thruster as a sensor for tracking of the focal spot on the absorber. This section

presents two algorithms used in determining the location of the focal spot using the absorber as the primary sensor. Both algorithms utilize concepts developed from studies of the Shack-Hartmann wavefront sensor. The first algorithm described uses correlation and masking for locating and tracking the focal spot. The second algorithm simplifies the method in algorithm one to using area moments for tracking sunlight.

ALGORITHMS:

METHOD ONE:

The image processing portion of the focus control system was developed along two paths. The first method to be discussed is the more general method using correlation, while the second method is less general based on area moments and area centroids similar to one version of the Shack-Hartmann analysis. The flow chart in Fig. 21 shows the sequence to be implemented for solar concentrator focus control.

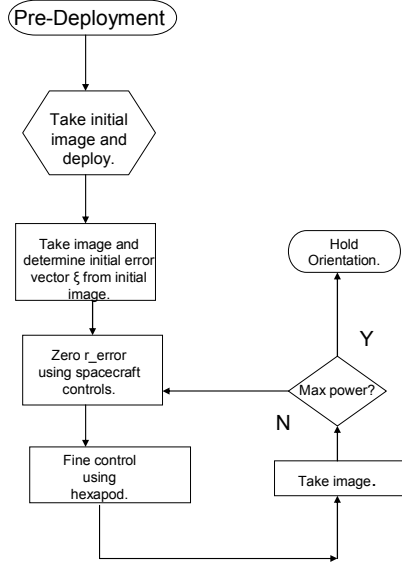


Figure 21 Flow Chart of Sequence.

Fig. 22 illustrates the diagram for the derivation of the correlation method of focal spot tracking. The method to be described here assumes that the concentrator and camera have been deployed into a configuration that has the concentrator pointing towards the Sun and the camera pointed at the thruster (absorber). The focal spot is located in the general area of the sensor but not on the optimized spot and that the system is not thrusting. Thus, after deployment and coarse alignment, the camera is pointed at the absorber and the concentrator is positioned facing the Sun. This situation is then defined as the initial position for the control algorithms Fig. 23. With

the addition of a stored image of the absorber in the on-Sun and on focus designed and geometric configuration, the control algorithms begin.

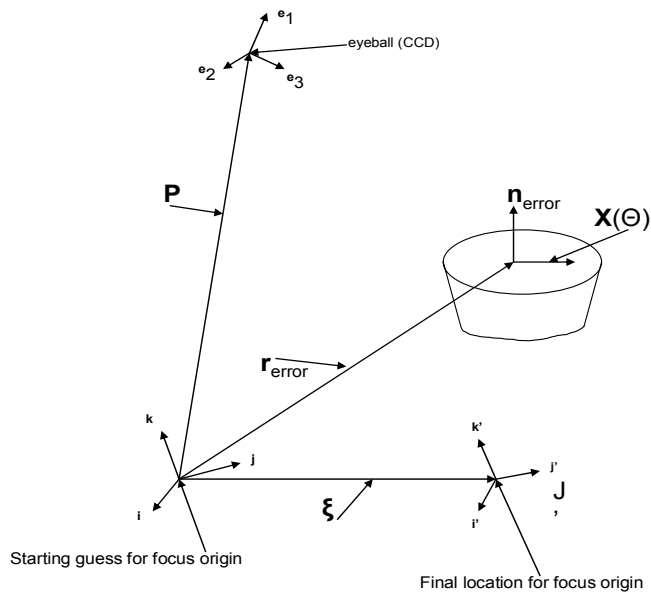


Figure 22 Coordinate System After Deployment

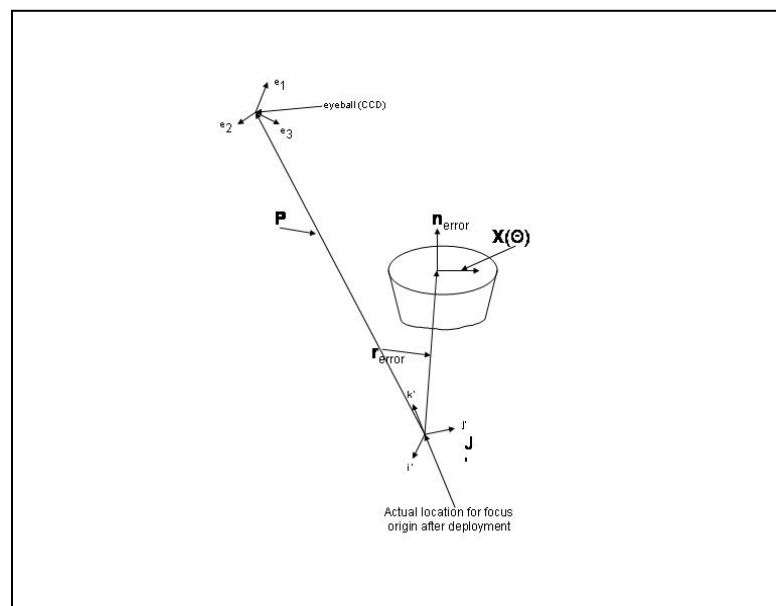


Figure 23 Coordinate System At Start, Fine Focus Control

At the start of the control program, the control computer has the initial configuration and initial image in memory. These initial conditions also define an initial coordinate system as displayed in Fig. 23. Also stored in the control computer are masks to be used in computing where the focal spot is currently located each iteration. The correlation or the lack of correlation at the masked areas indicates the current location of the spot and indicates the direction of travel required to reduce the mismatch. The overall process for this control algorithm follows image correlation or scene matching from computer pattern recognition [9], [10]. Both procedures follow a similar mathematical development to that of correlation between masked areas of the test image with the image of the on focus image. Optimization is utilized to find the optimal and correct focal spot location.

From Fig. 22, \vec{r}_{error} , \vec{p} , $\vec{X}(\theta)$, and \vec{n}_{error} are the primary vectors in the development of the algorithms. When the system is deployed on orbit, the initial position of the concentrator, camera, and thruster determine the initial origin and coordinate system. \vec{r}_{error} is the vector that determines the location of the image in the original coordinate system for the focus spot. \vec{n}_{error} is the vector

normal to the plane at the current image location at \vec{r}_{error} .

\vec{p} is the location of the camera or "eye-position" with respect to the original coordinate system. Finally, $\vec{X}(\theta)$ is defined as the vector representing areas of the images that are located in regions of interest. The regions of interest in the case of these algorithms would be the thruster itself or the individual rings of the absorber. The required accuracy of focal spot location determines whether the thruster as a whole would be the region of interest or the individual rings.

After deployment, the coarse focus system works to reduce the error vector, $\vec{\xi}$, to the position presented in Fig. 23. Once in the configuration of Fig. 23, the fine focus mechanism begins for the reduction of the vector \vec{r}_{error} to steer the concentrator to optimum spot location.

For the imaging portion of the process, the vector $\vec{X}(\theta)$ in the proceeding paragraph would have to be projected onto the CCD camera image plane. The method used for this operation is based on pinhole optics and perspective projection. The CCD camera utilizes a small aperture larger than a pixel for its near infinite depth of field. A lens is positioned just behind the pinhole to focus the pinhole

image onto the CCD matrix in the camera. With these optical parameters the projection of $\vec{X}(\theta)$ onto the CCD matrix with coordinates (a,b) is determined using the following equations.

$$a(\theta) = \alpha * \left(\left(\vec{X}(\theta) + \vec{r}_{error} - \vec{p} \right) \bullet \hat{e}_1 \right) / \left(\vec{X}(\theta) + \vec{r}_{error} - \vec{p} \right) \bullet \hat{e}_3 \quad (1)$$

$$b(\theta) = \beta * \left(\left(\vec{X}(\theta) + \vec{r}_{error} - \vec{p} \right) \bullet \hat{e}_2 \right) / \left(\vec{X}(\theta) + \vec{r}_{error} - \vec{p} \right) \bullet \hat{e}_3 \quad (2)$$

α and β in 1 and 2 are scaling factors determined by the CCD pixel size. The \hat{e} vectors are unit vectors located at \vec{p} defining a coordinate system at \vec{p} for the camera.

Now that the image and system coordinates and vectors have been defined, the correlation function is derived. The image taken by the CCD will be denoted $I(a, b)$ and is a function of (α, β) as expected. $W(\alpha, \beta)$ will represent the image or sub-image that we are trying to match. For example, $W(\alpha, \beta)$ would represent the ideal on focus image or it could represent only a portion of the ideal image such as specific rings of the sensor. The L_2 norm will then be utilized to calculate the minimum distance between $W(\alpha, \beta)$ and the current image.

$$E(m, N) = \left(\sum_{j=1}^J \sum_{i=1}^I [I(i+m-1, j+n-1) - W(I, j)]^2 \right)^{0.5} \quad (3)$$

Where $E(m, n)$ in 3 is the measure of distance at coordinates (m, n) .

Equation 3 also assumes that W is smaller than the image I , but that does not preclude using a W that is equal to I in size. Square and expand both sides of 3 while using the assumption that the energies in W and I are constant and very small, the correlation of W and E results as shown in 4.

$$E^2(m, n) = -2 * \sum_{j=1}^J \sum_{i=1}^I I(i+m-1, j+n-1) * W(i, J) \quad (4)$$

Multiplying 4 by $-1/2$ generates the correlation $R(m, n)$ at (m, n) as shown in 5.

$$R(m, n) = \sum_{j=1}^J \sum_{i=1}^I I(i+m-1, j+n-1) * W(I, j) \quad (5)$$

Finding the maximum value for $R(m, n)$ will determine the best location in the image that matches W . Finding the X, Y location of the maximum value for $R(m, n)$ and determining the difference from that location to the location of the autocorrelation of the on focus image determines which

direction to move the image to match the maximum correlation. Once the difference between the autocorrelation of the on focus image location and the point of maximum correlation is found, the control system would move the concentrators to reduce this difference. Equation 5, correlation was thought to be sufficient for determining the location of the focus.

MASKS:

Several different masks were generated, using a free hand drawing method, to determine which style of masks to use for determining the focal spot location. Best in this usage means that the masks were best suited to determining the offset distance from the focus location. Several masks that were used with the tubular absorber are shown in Fig. 24, Fig. 25, and Fig. 26. Similar masks were used with the loop of tubing that replaced the absorber for testing. The difference in the masks was which ring of the absorber was used in preparing the mask. For the outer ring mask, the outermost ring of the absorber was used as the masking area and thus enclosed a bigger area of the image than that covered by the inner ring mask. So although the masks in Fig. 24 and Fig. 25 look alike, they, in fact, cover very

different regions of the images. The mask in Fig. 26 was thought to be able to isolate a portion of the outer ring for consideration. In actual practice, it matched too many intensity levels to be of use, especially once the light got less than 4 diameters off of focus. In other words, Fig. 26 could not be used to discriminate below about 4 diameters as its correlation was smeared and did not produce impulse-like behavior at correlation.

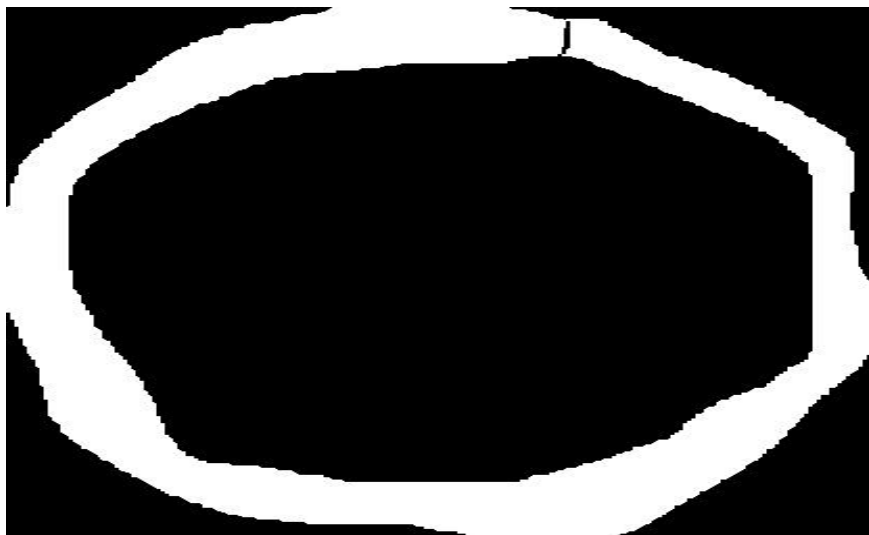


Figure 24 An Inner Ring Mask

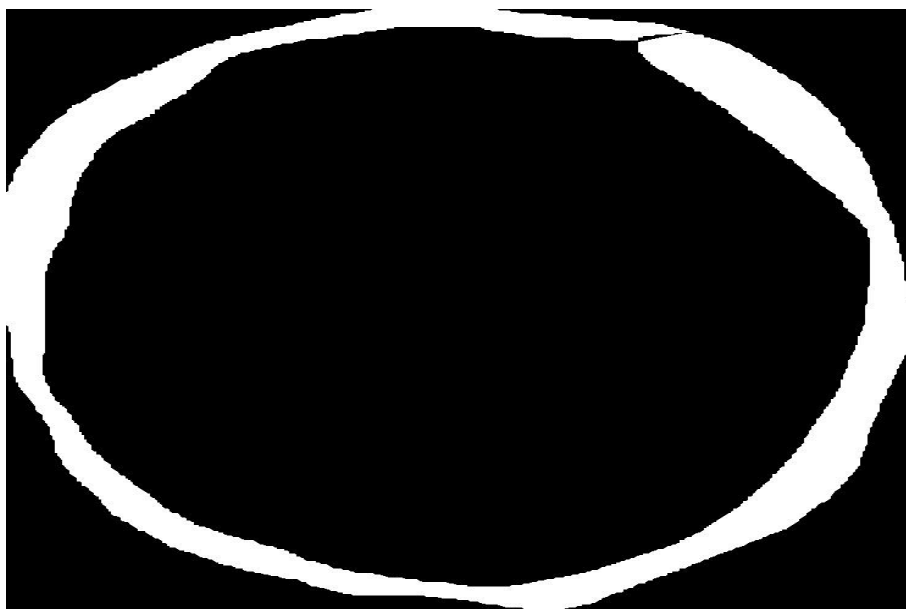


Figure 25 Outer Ring Mask



Figure 26 "Banana" Shaped Mask

METHOD TWO:

The second method for determining focal spot location is by measuring light area moments in the image. This method is derived based on a modification of the Shack-Hartmann wave front sensor using cylindrical mirrors instead of lenslets to register light areas [11]. Images of the concentrator can be seen in each coil of the absorber. Whether a particular image on the tube, denoted as a "tube blob" is bright or dim depends on how close the tube is to the focal point. Image area moments are then used to quantify focus for individual "tube blobs." The derivation also follows from a discussion of area moments and centroids from mechanics [12]. An image is acquired via the CCD camera and a threshold is applied to the image for further processing.

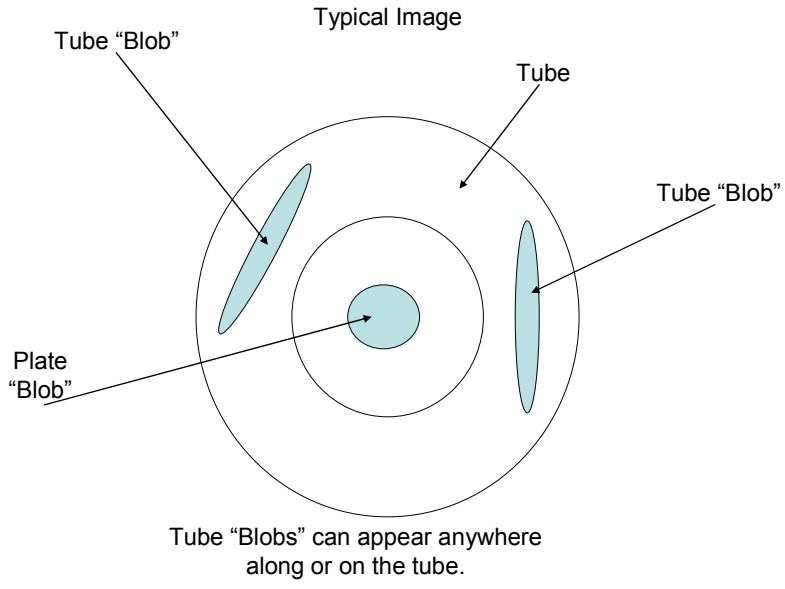


Figure 27 Generic Light Images On Tubes Of Sensor

Fig. 27 shows a generic schematic of light blobs from an image of the sensor. As explained earlier, each tube "blob" is an actual image of the light from the concentrator. The shape and intensity area of each tube blob is related to the amount of light in the concentrator being concentrated to that area of the tube. Calculating the area centroid of the images in the tubes determines where the focal spot is located on this iteration of the algorithm. Knowing where the centroid of the focal spot is located for this iteration determines which direction the control algorithm needs to move the concentrator to move the centroid to the center of the sensor.

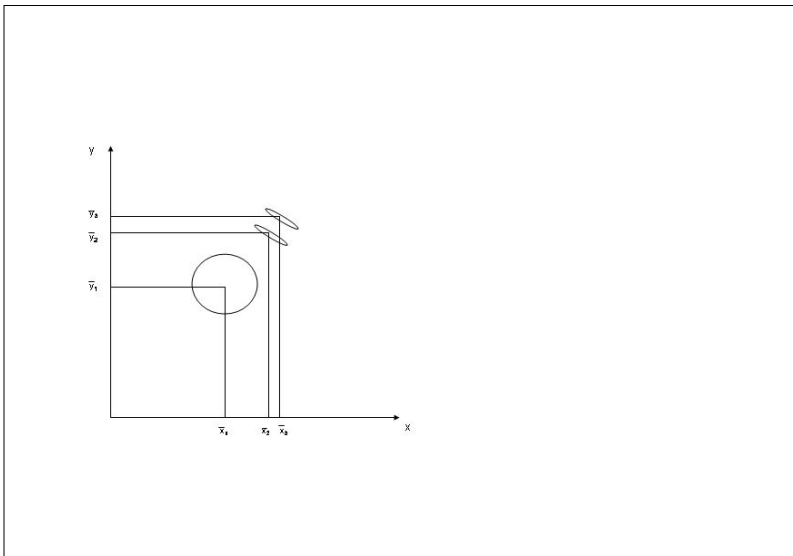


Figure 28 Light In Image From CCD

Fig. 28 shows the situation that might occur once the CCD acquires an image. A coordinate system for the image is setup as shown in Fig. 28. The image is then processed by first thresholding the image and then calculating the area moments for each light area. The threshold is set, at least in the ground experiments, by visually making sure that the lighted areas in the sensor tubes do not overlap into the area of the secondary concentrator. On flight another method of preventing overlap would be needed, possibly a measured area of the absorber beyond which the controller would ignore. Once the image has been thresholded, the area moments are calculated and an average

or overall centroid is calculated as the location of the focal spot on the sensor.

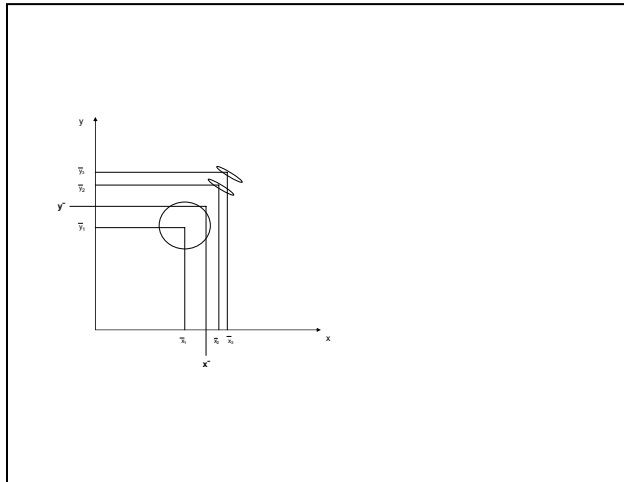


Figure 29 Centroid Calculation

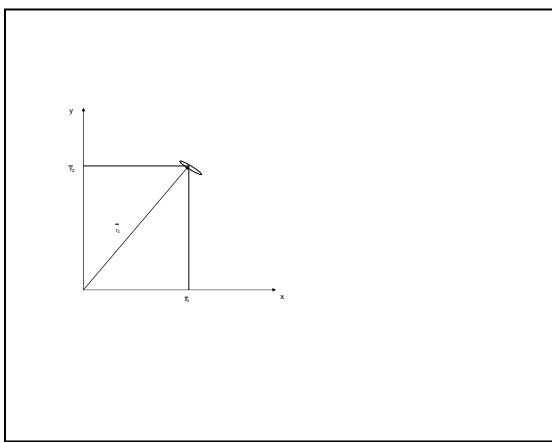


Figure 30 Calculation Schematic

Fig. 30 is an ideal schematic of the calculation for one of the ellipse shaped light areas. The light area is located at \vec{r}_2 and the area calculated as $(\pi*a*b)/4$, where (a) is the major axis of the ellipse and (b) is the minor axis of the ellipse. Position vector \vec{r}_2 is the vector from the origin to the center of the ellipse.

Finally, Fig. 29 shows the calculations shown in Fig. 28 and Fig. 30 combined to calculate the overall area centroid. As shown in Fig. 29, the image of the central flat plate will have a significant "blob" of light located at the center of the sensor as the control described in this paper assumes a coarse focus is obtained before the methods of this paper are used for fine focus. If the "blob" of light in the center of the image is too big for the area centroids to be calculated, it can be suppressed in the calculation of centroids to obtain locations that are very close to focus.

IMAGEJ AND IMAGE ANALYSIS[13]

The ImageJ image analysis and processing package from the National Institutes of Health was used to process the images taken in the experiments. The program provides a graphical user interface or GUI and extensive image analysis commands. ImageJ is also extendable by using either macros or ImageJ plugins. Plugins are basically Java classes that implement one of several interfaces in ImageJ or they are Java classes performing specific operations within ImageJ.

METHOD 1

ImageJ performs correlation on images using the conjugate multiplication of the Fourier transforms of two images to be correlated. Masks were utilized to reduce the size of images to include only specific tubes of the absorber area as the region of interest. Masking also helped the processing time required for the calculation of the FFTs as the images were reduced from 2184X1472 down to a more manageable 512 X 512 while still maintaining the correct region of interest.

Results from the processing of various offsets from on focus are presented in Fig. 31 through Fig. 33.

Fig. 32 shows the autocorrelation result for the on focus image. It has a very clear "dot" or impulse at the center of the image. This result was expected as the autocorrelation of an image with itself would be an impulse at offset (0,0).

Fig. 31 shows the result for the cross-correlation between the images for up 1 diameter from on focus of the solar simulator and the on focus. In this instance, the correlation is smeared and basically located at the center of the image indicating that the 1 diameter misalignment has not been resolved from the on focus situation in which the maximum value is located in the center of the image.

Fig. 34 shows a much better situation for the correlation technique. This figure shows the correlation between a 4 diameter image and the on focus image. This figure also shows the result for a mask similar to the one shown in Fig. 26. The mask used in Fig. 34 has other problems at a smaller offset as the numbers of correlations that may occur in the image get larger as the focus spot gets closer to the on focus location.

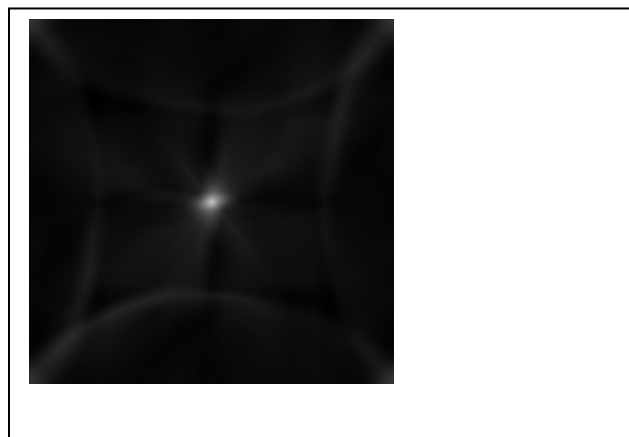


Figure 31 Correlation Up 1 Diameter

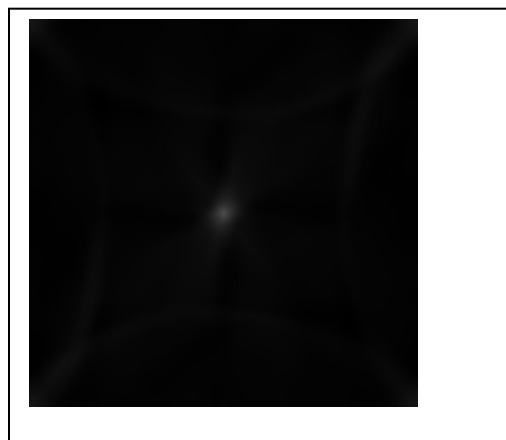


Figure 32 Autocorrelation



Figure 33 Correlation for 2 Diameter Offset

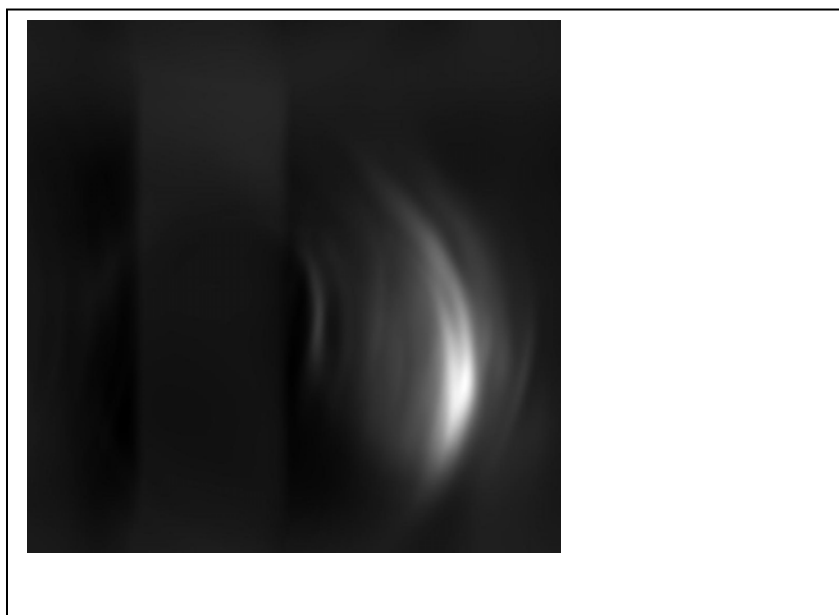


Figure 34 Correlation 4 Diameter Offset

The correlation shown in Fig. 33 illustrates the problems involved when using the correlation function at offsets below about 3 diameters. The correlation in Fig. 33 shows that an offset exists; however, the offset itself cannot be determined from this image. The cutoff for using masks like those in Fig. 24 and Fig. 25 using correlation defined by 5 appears to be between 2 and 3 diameters of offset.

However, at this point it was noted that using only 5 lead to problems as it would find any and all correlations based on the maximum intensities present, with little regard for the variations in intensities present in an area of the image, instead of the correct correlation value. That is, 5 would pick an area in $I(m,n)$ that in general had very high intensities instead of actually the point of highest correlation. That problem is eliminated by dividing 5 by the total energy in $I(m,n)$, $(\sum_{j=1}^J \sum_{i=1}^I I^2(i+m-1, j+n-1))^{0.5}$. Furthermore, 5 can be normalized to the range $(-1, 1)$ by dividing by the energy in $W(m,n)$. It was not necessary to divide by the energy of $W(m,n)$ for the case being discussed in this paper as it was not important to get values from $(-1, 1)$. Another form for 5 is known as the phase only correlation that basically divides $W(m,n)$ by the magnitude of $W(m,n)$, which normalizes the FFT of W .

providing only the phase information which provides a more impulse-like function for the correlation. As a quick approximation of the phase only correlation, a high pass filtering was tried since the phase only equation is similar to 5 but with the addition of dividing by the magnitude of W . Dividing by the magnitude of W , with W having low pass frequency patterns, is approximately high pass. The result shown in Fig. 32 shows one application of the high pass filtering for the autocorrelation. The phase only correlation will be looked at in a future paper.

METHOD 2

ImageJ was also utilized for the analysis outlined in method two of this paper. The particular command used was the "Analyze Particles" of the Analyze menu. To prepare the images for analysis, each image had to have a threshold applied to them before "Analyze Particles" would work. For the experiments in this paper the automatic threshold was used for all images. It was felt that auto threshold would be fine for verifying the concepts and algorithms presented in this paper. Table one lists the various particles found in calculating the areas and centroids for each image examined. Particle analysis does not require masking so no masks are indicated. The label column describes the image

file which also presents the source positioning information for that image. For example the label "up0diam_1diam_pos_x..." indicates that the source light was positioned 1 diameter off of center in the positive X direction and was not moved vertically, etc. Fig.28 and Fig.35 present the corresponding coordinate axes for both the thruster and the source as used in Table 1.

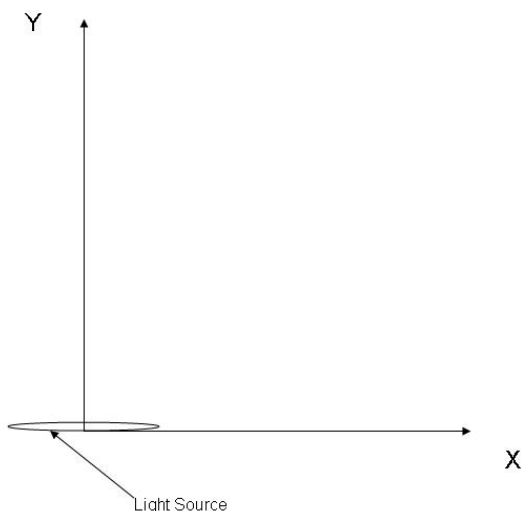


Figure 35 Source Coordinate Axes

	Label	Area	X	Y	Major	Minor	Angle
1	on_focus_pt5secs_4_aug_2005	4343	276.746	29.401	182.604	30.282	166.102
2	on_focus_pt5secs_4_aug_2005	16891	292.18	139.54	160.747	133.908	134.72
3	on_focus_pt5secs_4_aug_2005	1175	304.546	429.943	109.479	13.665	14.483

DRAFT

4	up0diam_1diam_pos_x_pt5secs_4_aug_2005	6187	185.416	35.906	183.007	43.066	11.87
5	up0diam_1diam_pos_x_pt5secs_4_aug_2005	27247	258.621	161.973	218.615	158.964	120.044
6	up0diam_1diam_pos_x_pt5secs_4_aug_2005	2705	203.531	424.335	166.181	20.733	164.91
7	up0diam_1diam_neg_x_pt5secs_4_aug_2005	3978	337.551	55.936	173.186	29.253	147.823
8	up0diam_1pt5inch_neg_x_pt5secs_4_aug_2005	5127	314.891	44.521	189.146	34.519	154.33
9	up0diam_1pt5inch_neg_x_pt5secs_4_aug_2005	6695	334.321	130.899	117.068	72.848	133.903
10	up0diam_1pt5inch_pos_x_pt5secs_4_aug_2005	5195	178.505	38.044	168.821	39.188	13.164
11	up0diam_1pt5inch_pos_x_pt5secs_4_aug_2005	28812	253.873	178.983	225.809	162.904	116.247
12	up0diam_1pt5inch_pos_x_pt5secs_4_aug_2005	3686	187.472	418.152	188.46	24.916	161.517
13	up0diam_2diam_neg_x_pt5secs_4_aug_2005	4431	375.153	86.678	182.028	30.994	135.517
14	up0diam_3diam_neg_x_pt5secs_4_aug_2005	4091	383.473	93.188	175.383	29.7	133.809
15	up0diam_2diam_pos_x_pt5secs_4_aug_2005	280	182.303	10.264	30.403	11.894	13.253
16	up0diam_2diam_pos_x_pt5secs_4_aug_2005	3431	69.194	94.311	150.213	29.099	52.783
17	up0diam_2diam_pos_x_pt5secs_4_aug_2005	22244	203.33	195.177	224.069	127.143	121.013
18	up0diam_2diam_pos_x_pt5secs_4_aug_2005	5181	86.968	354.649	210.627	31.325	138.272
19	up0diam_3diam_pos_x_pt5secs_4_aug_2005	1447	45.048	126.181	78.912	23.347	65.158
20	up0diam_3diam_pos_x_pt5secs_4_aug_2005	2634	28.036	295.441	139.366	24.064	119.143
21	up0diam_3diam_pos_x_pt5secs_4_aug_2005	211	176.264	252.713	24.213	11.358	113.949

Table 1 Images and Area Calculations with Centroids and Ellipse parameters.

The columns in Table 1 for major, minor and angle are the parameters for ellipses that approximate the areas of light in the images. These parameters were taken for future analyses that involve using the major axis and minor axis

values to determine shrinkage or elongation of the light areas that may be useful to increase the effectiveness of the area moment method for determining focal spot location. The angle parameter is related to the angle between the major axis of each ellipse and a line parallel to the horizontal or X axis in the image. The angle and the length measurements could be combined into the method of area moments to enhance the focal spot location determination.



Figure 36 On Focus Image For Area Moments.

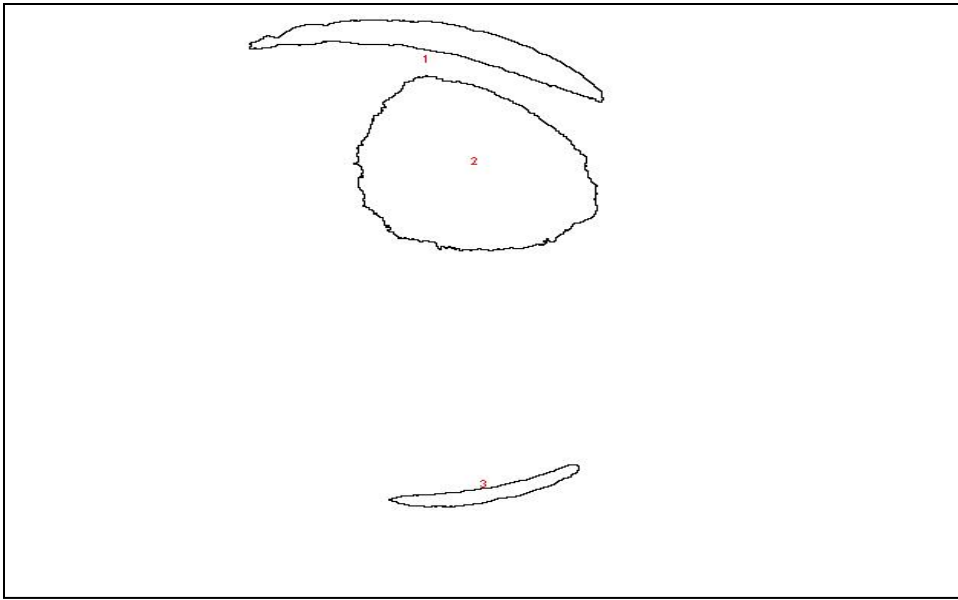


Figure 37 Particles From 36, Blobs 1 And 3 Are Concentrator Images On The Tubes.

Fig. 36 presents the situation in the process after the image has been cropped and a threshold has been applied. The next step in the process is shown in Fig. 37 when ImageJ has calculated the individual areas based on a minimum size of 100 pixels. The 100 pixel limit came from the fact that a 100 pixel area reduced the number of areas to work from and was calculated to be 3-5 percent of the approximately 2000 pixels on a tube blob for a fully lit concentrator on focus. Thus we ignored "tube blobs" that were smaller than 100 pixels signifying less than 5 percent of the concentrator lit. The values for the centroids and areas for the image shown in Fig. 33 are shown in table 1 with label

on_focus_pt5secs_4_aug_2005. Calculations for the image: up0diam_1diam_pos_x_pt5secs_4_aug_2005 gave an average X value of 194.473 and average Y value of 230.12. The method then uses either the centroid of the central "plate blob" of light or the centroid of the on focus image to generate the difference signal used for concentrator control. For the "tube blob" analysis, the difference calculation gives a $|X|$ difference of 64.148 and a $|Y|$ difference of 68.147. By subtracting the focal spot centroids from the centroid of the "blob" a direction of movement towards focus is generated. If the on focus X and Y centroids are retained from that image a larger displacement value may be generated for the control values that move the focal spot towards focus. When there is no central "plate blob" of light in the image, the centroids for X and Y from the on focus image have to be used for delta calculations. These delta calculations would then be used to generate control values for the hexapod controller. Looking at Fig. 38, it can be seen that this method works down to at least 1.5 inches off of focus for the solar simulator. That number is associated with 0.15 degrees of offset, which is very close to the arbitrary requirement that we control to 0.1 degree.

Centroid Results							
	Label	Area	X	Y	Major	Minor	Angle
1	on_focus_pt5secs_4_aug_2005	4343	276.746	29.401	182.604	30.282	166.102
2	on_focus_pt5secs_4_aug_2005	16891	292.18	139.54	160.747	133.908	134.72
3	on_focus_pt5secs_4_aug_2005	1175	304.546	429.943	169.479	13.665	14.483
Averages		291.157	199.628				
4	up0diam_1diam_pos_x_pt5secs_4_aug_2005	6187	185.416	35.906	183.007	43.066	11.87
5	up0diam_1diam_pos_x_pt5secs_4_aug_2005	27247	258.621	161.973	218.615	158.964	120.044
6	up0diam_1diam_pos_x_pt5secs_4_aug_2005	2705	203.531	424.335	166.181	20.733	164.91
Averages		215.856	207.405				
Differences (On - 1diam)		73.301	-7.777				

Figure 38 Centroid Results.

SUMMARY AND CONCLUSIONS:

A system was needed to provide focus control for solar concentrators used in the high temperature environment of terrestrial and space applications. The system discussed in this paper performs this application superbly. A well known and used method of measuring imperfections in telescopes, Shack-Hartmann wave front sensor and in the current case, an absorber, was modified and algorithms were developed to use in the control portion of the system developed. The algorithms were developed using ImageJ for processing and analyzing the camera images.

The two algorithms developed were the masking/correlation and the area moment algorithms. Both methods work for locating the focal spot on the sensor down to about 2-3 Sun simulator diameters off of alignment. This amount of misalignment corresponds to 6-9 inches off of alignment of the simulator in the experiment. The 6-9 inches of offset corresponds to 0.6 to 0.9 degrees of angle of misalignment. Correlation using only 5 fails to work below 2-3 diameters of misalignment. Area moments did better below 2-3 diameters of misalignment. Table 1 shows the complete calculation for an image with the Sun simulator 1 diameter of focus. Good focal spot tracking was seen from 5 diameters of misalignment down to 1.5 inch of misalignment. The 1.5 inch gives about 0.15 degree of misalignment using the 1 X 2 meter concentrator, which is very close to our original arbitrary requirement.

The system as developed in this paper solves the high temperature problem and gives two algorithms to determine focal spot location.

FUTURE WORK:

Future work will include automating, using ImageJ, the steps outlined in this paper to control either a model of

the concentrator and thruster or an actual concentrator with hexapod and thruster. Another area for future work is modifying ImageJ's FFT Math process to implement the phase-only correlation to improve the correlation algorithm to operate with the source light below 2-3 diameters off of focus. Also, a combination of both methods should be studied to overcome the limitations of the correlation method. Finally, data should be taken below 1.5 inches of misalignment to verify that the method can get to the .1 degree of misalignment and improve the control down to 0.02 degrees of misalignment where the thruster acceleration could be utilized in the optimization of concentrator location using a combination of POC and area moments or a refined area moment method.

DRAFT

REFERENCES

- [1] Holmes, Dr. Michael R., "Ideal Performance of Off-Axis Paraboloid Concentrators for Solar-Thermal Propulsion," ASME 1996
- [2] IBID.
- [3] Wassom, Dr. Steven R., "Focus Control System for Solar Thermal Propulsion," 2000 International ADAMS User Conference.
- [4] Dickinson, William C., Paul N. Cheremisinoff, Solar Energy Technology Part A, Engineering Fundamentals, Marcel Dekker, Inc., New York, New York, 1980.
- [5] Hulstrom, Roland L., Solar Resources, The MIT Press, Cambridge, Massachusetts, 1989.
- [6] Shack, Roland, Dr., Ben C. Platt, Ph. D., "History and Principles of Shack-Hartmann Wavefront Sensing." Journal of Refractive Surgery, Vol. 17, September/October 2001.
- [7] IBID.
- [8] Beasley, Joseph N., "A Novel Wave Front Method Used for Tracking Terrestrial Concentrator Focal Spot Location," 2004 JANNAF Conference.
- [9] Wong, Robert Y., Computer Pattern Classification and Scene Matching., The Faculty Press, California State University, Northridge, CA, 1981.
- [10] Dudzik, Michael C. ed., Electro-Optical Systems Designs, Analysis, and Testing. Volume 4, 2nd ed., Ann Arbor , Michigan: Infrared Information Analysis Center Environmental Research Institute of Michigan., Bellingham, Washington: SPIE Optical Engineering Press., 1996.
- [11] Tokovinin Andrei A., "Tutorial on Adaptive Optics at CTIO", <http://www.ctio.noao.edu/~atokovin/tutorial/index.html> , Cerro Tololo Inter-American Observatory, July 10, 2001.
- [12] Hibbeler, R. C, Engineering mechanics, statics. Macmillan Publishing Co., INC, New York, New York, 1978.

DRAFT

[13] Rasband, W. S., ImageJ, U. S. National Institutes of Health, Bethesda, Maryland, USA,
<http://rsb.info.nih.gov/ij/>, 1997-2005.